Effects of Megasplay Fault Activity on Earthquake Hazards: Insights from Discrete Element Simulations

Wang Xiaoyu[1] and Morgan Julia[1]

[1]Rice University

November 16, 2022

Abstract

Deep-water megasplay faults may promote or limit earthquake rupture and tsunami genesis. To better understand how megasplay faults affect earthquake rupture and associated tsunami potential, we build on recent modeling efforts based on observations of coseismic ruptures in the Japan Trench forearc and Chile Margin. We model the upper plate as a wedge that is partitioned into a seismic (velocity-weakening) inner wedge and an outer aseismic (velocity-strengthening) wedge, combined with a splay fault rooting from the decollement. We examine the effects of dip and friction along the splay fault and the width of the outer (velocity-strengthening) wedge during earthquake rupture. Our results suggest that along-strike variations in width of the velocity-strengthening outer wedge along the Chile Margin may play a key role in splay fault activity in the rupture segment of the 2010 Maule earthquake. However, our model fit to the published slip distribution for the 2010 Maule earthquake, suggests that megasplay fault activation did not significantly impact earthquake size along the SC Chile Margin. In contrast, our model fit to the slip distribution for the 2011 Tohoku earthquake shows that megasplay fault reactivation may have moderately affected earthquake coseismic rupture. Splay faults can slip coseismically thus contributing to associated tsunamis. However, the presence of a velocity-strengthening outer wedge is the predominant constraint on rupture size and tsunami generation.

Posted on 16 Nov 2022 — CC-BY-NC-ND 4 — https://doi.org/10.1002/essoar.10507865.1 — This a preprint and has not been peer reviewed. Data may be preliminary.

Journal of Geophysical Research

Supporting Information for

Implication of Splay Fault Activity for Megathrust Earthquake Hazards: Insights from Discrete Element Simulations

Xiaoyu Wang[1], Julia K. Morgan[1]

[1] Department of Earth, Environmental and Planetary Sciences, Rice University, Houston, Texas, USA.

Introduction

This supporting material introduces the basics of the discrete element method (DEM), the experimental model setup, and simulation workflow. Moreover, we tabulate the important mechanical and numerical parameters used to build the initial models.

Text S1. DEM Modeling

In our implementation of the discrete-element-method (DEM), we simulate an assemblage of discrete spherical particles that interact with each other according to elastic-frictional (Hertz-Mindlin) contact law. We introduce cohesion by adding a mechanical bond at interparticle contacts (Morgan, 2015). This property can allow us to simulate cohesive materials as may occur within the deeper accretionary prism. The more frontal region of a prism is approximated as non-cohesive, i.e., lacking interparticle bonds. The combination of pre-assigned interparticle contact parameters, in combination with the mechanical properties of the particles themselves, define the overall behavior of the particle assemblage. This study uses a version of DEM implemented in RICEBAL. Details about the method are provided in Morgan and Boettcher (1999), Guo and Morgan (2004; 2006), and Morgan (2015). Continuum approximations of the bulk properties and behavior of the numerical model are derived using the contact force distribution and displacement gradients. By averaging continuum properties over finite volumes, stress and strain fields can be calculated for the domain (Thornton and Barnes, 1986; Morgan and Boettcher, 1999; Morgan and McGovern, 2005a; 2005b; Morgan, 2015).

Figure 1 shows the general model setup. The initial length of the simulated wedge is set to 200km, comparable to the dimensions of the rupture lengths along the Chile Margin (Moreno *et al.* , 2010; Contreras-Reyes *et al.* , 2017). To best balance model run time and model resolution, the upper wedge is constructed of approximately 200,000 discrete particles with radii of 100, 120, 160 and 200 m. Particles are randomly generated within a two-dimensional domain 400×60 km, allowed to settle under gravity, and then trimmed to the desired wedge geometry.

The mechanical properties of the simulated system are defined by the assigned particle properties and interparticle friction coefficients (Table S1 and Table S2). The gray particles defining the basal sliding surface are fixed in space, their small radii (10 m) ensure a relatively smooth sliding surface, unimpeded by particle roughness.

The contacts between particles, distinguished by labeled surface types (Figure 1), is controlled by the interparticle friction coefficients. The basal sliding surface is defined by Surface Type 4. The upper plate as is partitioned into an inner (velocity-weakening) wedge (Surface Type 1) and outer (velocity-strengthening) wedge (Surface Type 3) domains. The splay fault boundary defined by Surface Type 1 and Surface Type 2. In addition, cohesiveness, as an option, can be implemented by adding bonds to every contact to simulate more realistic cohesive material. The mechanical properties of the domain and the fault interface are controlled by the particle properties and interparticle friction coefficients. To simulate a predefined fault, relatively low or zero interparticle friction coefficients can be assigned to the particles that define the fault interface, with no cohesion at the contacts between those particles.

Text S2. Simulation Workflow

We seek to simulate the dynamic Coulomb Wedge model earthquake cycle (Wang and Hu, 2006) in our simulations. We first prepare the fault for dynamic slip by preconditioning it during steady backwall displacement, holding the initial basal friction at 0.04. This represents the interseismic stage. This preconditioning ensures high shear stress along the fault and the accumulation of elastic strain energy within the wedge. To simulate the dynamic stage of the earthquake cycle, we reduce the friction coefficient along the basal decollement beneath the inner wedge to approximate velocity weakening and either increase or maintain the basal friction beneath the outer wedge to approximate velocity strengthening. the internal friction coefficient is maintained at 0.30 for both the inner and outer wedges.

During the pre-earthquake loading stage, the right wall of the wedge moves inward at a constant horizontal velocity (v_x) of 1 m/s, under constant basal friction conditions. During this preconditioning stage, the system state is recorded at increments of 200 m of backwall displacement. The internal stresses within

Posted on 16 Nov 2022 — CC-BY-NC-ND 4 — https://doi.org/10.1002/essoar.10507865.1 — This a preprint and has not been peer reviewed. Data may be preliminary.

the wedge are supported by elastic deformation at interparticle contacts, defining the potential energy of the system. During this stage, the wedge deforms, either extending or contracting, depending on the basal friction conditions and the predefined wedge geometry. The preconditioning stage is complete when the model reaches its steady state, State 1. Details about the implementation of preconditioning and the discussion about the steady state can be found in Wang and Morgan (2019).

Once the wedge reaches State 1, we simulate the second stage of dynamic earthquake unloading, culminating in the final State 2. At the start of the second stage, backwall displacement is stopped. Earthquake unloading is initiated by the reduction in basal friction beneath the inner wedge, and concurrent increase in friction beneath the outer wedge as appropriate.

For each model, a splay fault with a dip, varying from landward to seaward dipping is prescribed just before the earthquake unloading. A model without any prescribed splay fault is also constructed as a reference.

Table S1 Basal Friction Conditions along Megathrust and Splay Fault before and after Earthquake Unloading.

Experiments
Setup 1 Non-cohesive Models with ratios of outer wedge from 0% to 25% and dips ranging between landward 10° to seawa
Setup 2 Cohesive Models for Chile Margin and Japan Trench

Table S2 Model Parameters Used in the Simulation.

Dimensions of 2D Domain	400 km x 60 km
Young's Modulus for Particle (E_{particle})	2.9 E09 Pa
Particle Radii (r)	100, 120, 160, 200 m
Poisson's Ratio for Particle (v_{particle})	0.2
Density for Particle (ρ_{particle})	2500 kg/m^3
Young's (Normal) Modulus for Bond (E_{bond})	2E08
Shear Modulus for Bond (G_{bond})	2E08
Tensile strength for Bond (T_{0_bond})	4E07
Shear Strength for Bond (S_{0_bond})	8E08
Time Step/Cycle	0.05 sec/cycle
Number of Cycles/ Increment	4000 in preconditioning stage;
Rate of Backwall Displacement	1 m/s in preconditioning stage; 0 m/s in dynamic weakening stage.

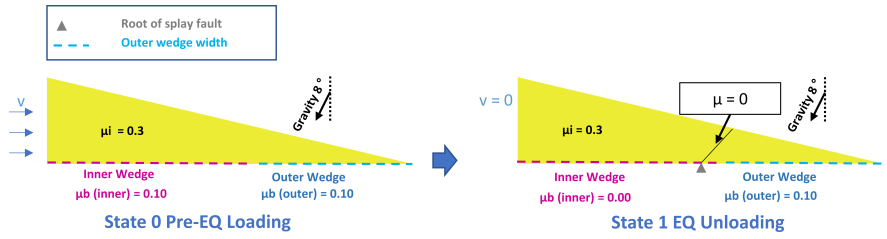

Posted on 16 Nov 2022 — CC-BY-NC-ND 4 — https://doi.org/10.1002/essoar.10507865.1 — This a preprint and has not been peer reviewed. Data may be preliminary.

Figure S1. Simulation workflow for Setup 1 (refer to Text S2).

Reference

Guo, Y., and Morgan, J. K. (2004), Influence of normal stress and grain shape on granular friction: Results of discrete element simulations,*Journal of Geophysical Research: Solid Earth* , *109* (B12).

Guo, Y., and Morgan, J. K. (2006), The frictional and micromechanical effects of grain comminution in fault gouge from distinct element simulations, *Journal of Geophysical Research: Solid Earth* ,*111* (B12).

Morgan, J. K. (2015), Effects of cohesion on the structural and mechanical evolution of fold and thrust belts and contractional wedges: Discrete element simulations, *Journal of Geophysical Research: Solid Earth* , *120* (5), 3870-3896.

Morgan, J. K., and Boettcher, M. S. (1999), Numerical simulations of granular shear zones using the distinct element method: 1. Shear zone kinematics and the micromechanics of localization, *Journal of Geophysical Research: Solid Earth* , *104* (B2), 2703-2719.

Morgan, J. K., and McGovern, P. J. (2005a), Discrete element simulations of gravitational volcanic deformation: 1. Deformation structures and geometries, *Journal of Geophysical Research: Solid Earth* ,*110* (B5).

Morgan, J. K., and McGovern, P. J. (2005b), Discrete element simulations of gravitational volcanic deformation: 2. Mechanical analysis,*Journal of Geophysical Research: Solid Earth* , *110* (B5).

Thornton, C., and Barnes, D. (1986), Computer simulated deformation of compact granular assemblies, *Acta Mechanica* , *64* (1-2), 45-61.

Wang, K., and Hu, Y. (2006), Accretionary prisms in subduction earthquake cycles: The theory of dynamic Coulomb wedge, *Journal of Geophysical Research: Solid Earth* , *111* (B6).

Wang, X., and Morgan, J. K. (2019), Controls on Fore-Arc Deformation and Stress Switching After the Great 2011 Tohoku-Oki Earthquake From Discrete Numerical Simulations, *Journal of Geophysical Research: Solid Earth* , *124* (8), 9265-9279.

Posted on 16 Nov 2022 — CC-BY-NC-ND 4 — https://doi.org/10.1002/essoar.10507865.1 — This a preprint and has not been peer reviewed. Data may be preliminary.

Effects of Megasplay Fault Activity on Earthquake Hazards: Insights from Discrete Element Simulations

Xiaoyu Wang[1], Julia K. Morgan[1]

[1] Department of Earth, Environmental and Planetary Sciences, Rice University, Houston, Texas, USA.

Corresponding author: Xiaoyu Wang (wangxy1987@gmail.com)

Key Points:

- The width of the velocity-strengthening outer wedge controls splay fault activity during earthquakes.
- The effect of megasplay faults on rupture extents and tsunami genesis is limited during seismic events.
- Variations in basal friction along the megathrust fault are the predominant control on the earthquake hazard.

Keywords

megasplay fault, discrete element, numerical simulation, tsunami potential, megathrust earthquake

Abstract

Deep-water megasplay faults may promote or limit earthquake rupture and tsunami genesis. To better understand how megasplay faults affect earthquake rupture and associated tsunami potential, we build on recent modeling efforts based on observations of coseismic ruptures in the Japan Trench forearc and Chile Margin. We model the upper plate as a wedge that is partitioned into a seismic (velocity-weakening) inner wedge and an outer aseismic (velocity-strengthening) wedge, combined with a splay fault rooting from the decollement. We examine the effects of dip and

friction along the splay fault and the width of the outer (velocity-strengthening) wedge during earthquake rupture. Our results suggest that along-strike variations in width of the velocity-strengthening outer wedge along the Chile Margin may play a key role in splay fault activity in the rupture segment of the 2010 Maule earthquake. However, our model fit to the published slip distribution for the 2010 Maule earthquake, suggests that megasplay fault activation did not significantly impact earthquake size along the SC Chile Margin. In contrast, our model fit to the slip distribution for the 2011 Tohoku earthquake shows that megasplay fault reactivation may have moderately affected earthquake coseismic rupture. Splay faults can slip coseismically thus contributing to associated tsunamis. However, the presence of a velocity-strengthening outer wedge is the predominant constraint on rupture size and tsunami generation.

Plain Language Summary

At subduction margins, the deep-water megasplay faults that cut the upper plate, may be reactivated during large coseismic ruptures, contributing to the generation of transoceanic tsunamis. The Mw 8.8 2010 Maule and Mw 9.1 2011 Tohoku earthquakes suggest that the megasplay faults may slip coseismically, contributing to subsequent tsunamis. However, the recent Mw 7.8 Simeonof and Mw 8.2 Chignik earthquakes offshore Alaska imply that the presence of such splay fault may not be necessarily indicative of strong tsunami potential. It is still not clear how megasplay fault activation and its interaction with slip along the megathrust fault affect the local seismic hazard assessment. In this work, we used the Discrete Element Method to model megasplay faults interpreted from subduction margins. Our models demonstrate that along-strike variations in the width of the velocity-strengthening outer wedge along the margin play a key role in splay fault activity in the rupture segment. Our simulation results show that the effect of the megasplay fault on rupture extents and tsunami genesis is limited for both the 2010 Maule and 2011 Tohoku earthquakes. However, the presence of a frictionally resistant outer wedge is the predominant constraint on rupture size and tsunami generation.

1 Introduction

Pre-existing forearc structures may influence the seismic hazard potential (Polet and Kanamori, 2000; Wang and Tréhu, 2016; Bécel *et al.*, 2017; Olsen *et al.*, 2020). Key features include deep-water megasplay faults, which may be reactivated during large coseismic ruptures, contributing to the generation of transoceanic tsunamis (Moore *et al.*, 2007; Wendt *et al.*, 2009; Lotto *et al.*, 2019). The conditions under which megasplay faults promote or limit earthquake rupture and tsunami genesis, however, are still unclear.

Thrust megasplay fault systems may act as barriers to seismic rupture. As an example, activation of the thrust-type Santa Maria fault system (SMFS) along the Chile Margin, may have contributed to segmenting and limiting finite megathrust slip during the Mw 8.8 2010 earthquake (Melnick *et al.*, 2006; Melnick *et al.*, 2012). In contrast, normal megasplay faults may facilitate earthquake rupture and tsunami generation. One example is the apparent reactivation of a normal fault within the upper plate during the Mw 9.0 2011 Tohoku-oki earthquake (Ito *et al.*, 2011), The tsunami that accompanied that event caused severe damage along the coastline of Japan. The uplift and seaward displacement of the footwall of the splay normal fault may have contributed to the large horizontal displacement along the megathrust (Tsuji *et al.*, 2011; McKenzie and Jackson, 2012). Thus, the sense of fault slip (i.e., normal or thrust) likely controls both earthquake size and tsunami potential. This hypothesis, however, is not well understood and has not yet been carefully tested.

A structural configuration comparable to the one involved in the Tohoku earthquake is interpreted in the Shumagin Gap, offshore Alaska, where a normal-type megasplay fault may have been activated by seismic ruptures propagated from adjacent locked segments (Bécel *et al.*, 2017). The activation of the normal fault may have caused the large historic tsunami in the Shumagin Gap. Interestingly, Mw 7.8 Simeonof and Mw 8.2 Chignik earthquakes recently occurred in the vicinity of the Shumagin gap in July 2020 and July 2021 respectively, with epicenters close to that configuration. In contrast to the Tohoku earthquake, these two events only caused waves of less than a foot (Grassi, 2021; Ruppert and Gardine, 2021).

One potential controlling factor that may contribute to the difference between the tsunami genesis for the Tohoku earthquake and the recent Alaska earthquakes is the variation in properties of a pre-existing megasplay fault. The properties of the splay fault that can affect the earthquake and tsunami size may differ at different localities along the strike, which may be reflected by the

activity of the splay fault after the mainshock. A possible demonstration of this effect is along the SC Chile Margin, where forearc splay faults were activated by the great 2010 Maule earthquake in some segments of the rupture zone but not in adjacent ones (Lieser *et al.*, 2014).

Another plausible controlling factor that may affect the earthquake, tsunami size, and splay fault activations are variations in friction along the decollement at different localities (Wang *et al.*, 2021). Previous studies show a correlation between the aseismic outer wedge (velocity-strengthening zone) width and the coseismic rupture and stress transfer triggered by a great megathrust earthquake. During fault slip, velocity-weakening behavior beneath the seismic inner wedge enables earthquake rupture and inner wedge extension. In contrast, the presence of a velocity-strengthening outer wedge induces compressive stress at the aseismic/seismic transition zone, which suppresses the propagation of the coseismic ruptures (Wang and Hu, 2006; Wang *et al.*, 2021). This stress evolution may influence the sense of slip and the degree of reactivation along pre-existing splay fault in the forearc.

To assess the local seismic hazard, therefore, it may not be enough simply to determine the presence and properties of a megasplay fault, as we also must understand how outer wedge width controls the activation and sense of slip along the megasplay fault during a seismic event. Here, we build on previous numerical simulations of megathrust slip processes (Wang *et al.*, 2021) to examine the role of splay faults within the upper plate. This study is focused on 1) investigating the factors (i.e. friction conditions along megathrust and splay fault, dips) that control the activation and sense of slip (i.e., normal or thrust) of a splay fault; 2) better understanding how splay faults influence fault displacement and tsunami generation; and finally, 3) exploring the role of fault reactivation in determining the earthquake size and tsunami potential for the 2010 Maule earthquake and 2011 Tohoku-oki earthquake.

2 Approach and Methodology

2.1 DEM Modeling and Experimental Design

In this study, we use a Discrete-Element-method (DEM) based program, RICEBAL, to construct the models. Details about the DEM methodology can be found in the previous publications (Morgan, 2015; Wang and Morgan, 2019). We build on recent modeling efforts based on observations of extensional deformation in the Japan Trench forearc and Chile Margin (Wang

et al., 2021).The initial wedge is constructed by randomly generating particles within a two-dimensional domain and letting them settle under gravity (Figure 1). The assemblage of particles is then sculpted to the desired wedge shape with a starting taper angle of 10° (α+β), and subjected to gravity tilted at an angle of 8° from the vertical, simulating a fixed megathrust dip angle (β) of 8°. This reference configuration is comparable to published geometries for several subduction margins (Ito *et al.*, 2011; Maksymowicz, 2015; Wang *et al.*, 2019). The initial full width of the wedge is 200 km, a typical downdip rupture distance along the subduction margin (Moreno *et al.*, 2010; Moreno *et al.*, 2012; Wei *et al.*, 2012). Focusing on the first-order effects of splay fault properties on earthquake rupture and tsunami potential during an earthquake cycle, we employ constant values of basal friction across each of the inner wedge or outer wedge for a given simulation stage, ignoring the spatial and temporal variations that likely occur in nature. The friction coefficient along the splay fault also is held constant for a given simulation stage. To clearly investigate certain controlling factors, our simplified model employs a sharp updip transition at the inner and outer wedge boundary. Moreover, the downdip boundary of the upper plate is defined by a rigid backwall. We, therefore, do not simulate any downdip velocity strengthening in the downdip region (Wang *et al.*, 2021). Details about the setup and the preset parameters can be found in the supplemental materials (S1).

Each numerical simulation is carried out in two stages: pre-earthquake loading and dynamic rupture (Figure S1). During the first loading stage, the backwall is displaced at a steady rate, while the slip of the wedge is resisted by constant basal friction. This causes the build-up of elastic strain energy within the wedge and increased shear stresses along the megathrust. Stage 1 is terminated following 8 km of backwall displacement, when the fault is poised for failure. Before the dynamic rupture stage, a splay fault with a prescribed dip, ranging from landward to seaward dipping, is introduced. For each simulation, we assign one of four values of friction along the splay faults to assess the effect. Then, to simulate velocity-weakening during coseismic rupture (Stage 2), the basal friction is instantly decreased beneath the inner wedge, resulting in dynamic slip along the underlying fault. Concurrently, the basal friction beneath the outer wedge is maintained at the higher value, simulating a more resistant frontal wedge. Changes in geometry and stress in the system are documented through Stage 2 until the fault slip ceases. More information about the modeling workflow can be found in the supplemental materials (S2) and our previous work (Wang *et al.*, 2021).

Two sets of simulations are carried out to address two specific objectives: Setup 1 uses non-cohesive wedges to investigate possible controls on splay fault activation and seafloor uplift. In particular, the simulations examine whether the outer wedge (velocity strengthening zone) width influences the reactivation and sense of slip along pre-existing splay faults of different orientations. Setup 2 investigates the effects of both landward and seaward dipping splay faults with specific orientations on coseismic slip distributions and seafloor uplift. This fault configuration builds upon our previous study that used non-faulted cohesive wedges to reproduce the published slip distributions for the 2010 Maule earthquake and 2011 Tohoku-oki earthquake (Wang *et al.*, 2021). Here, we assess if the presence of splay faults, as interpreted by others (Melnick *et al.*, 2006; Tsuji *et al.*, 2011), yields significantly different slip distributions that might affect the coseismic rupture and tsunami potential for both the 2010 Maule rupture zone and the 2011 Tohoku rupture zone.

2.2 Setup 1: Effects of Outer wedge Width and Splay Fault Orientation

In our first experimental setup, non-cohesive models are constructed with pre-existing splay faults with different orientations, all of which root into the decollement at 50 km distance from the toe. Fault orientations range from 10° to 60° with landward dips, and 20° to 80° with seaward dips. Outer wedge widths range from 0% - ~25% of the full wedge length. In all models, the internal friction coefficient (μ'_{int}) was maintained at 0.30 for both the inner and outer wedges (Table S1). The effective basal friction coefficients for the inner and outer wedges, μ'_{bas_inner} and μ'_{bas_outer}, respectively, were both set to 0.10 at the start of the pre-earthquake loading stage. During the earthquake rupture phase, μ'_{bas_inner} was instantly decreased to 0.00 while μ'_{bas_outer} was maintained at 0.10. In all models, the splay fault is introduced just before earthquake unloading, allowing us to test the impact of coseismic slip along the fault on the earthquake size and surface deformation. Simulation results are compared to a reference model without a prescribed splay fault.

2.3 Setup 2: Effects of Fault Friction on Prescribed Splay Fault Orientations

The second experimental setup examines the effects of a splay fault on coseismic displacements and seafloor uplift for models designed based on structural interpretations for the 2010 Maule earthquake and 2011 Tohoku-oki earthquake (Tsuji *et al.*, 2011; Melnick *et al.*, 2012). To define more realistic properties for these systems, cohesion was introduced by adding bonds at

178 the contacts among particles within the initial wedge following particle deposition and wedge
179 sculpting. We employ the same mechanical parameters as in our previous study here (Wang *et al.*,
180 2021), which defined realistic configurations for these two settings. The friction coefficients are
181 tabulated in Table S1. As above, the splay faults are introduced into the models just before
182 earthquake unloading. The Maule models employ a seaward dipping fault of 80°, which is
183 positioned based on the seismic interpretation of Melnick *et al.* (2006). A range of fault friction
184 coefficients between 0.00 and 0.10 were tested. The Tohoku models use a landward dipping fault
185 of 30°, located based on the interpretations of (Tsuji *et al.*, 2011), again using the same range of
186 fault friction values as above. The widths of the higher friction outer wedge were fixed for these
187 models to match those used previously (Wang *et al.*, 2021), set to ~90 km from the toe for the
188 Maule models and less than 5 km from the toe for Tohoku models in the initial model setups.
189

190 **3 Results**

191 3.1 Effect of Outer Wedge Width on Stress Transfer and Splay Fault Activity

192 The first set of simulations using Setup 1 examined the effects of the width of the aseismic
193 outer wedge (velocity-strengthening zone) on stress transfer and splay fault activity. Landward
194 dipping or seaward dipping faults oriented at 45° are introduced just prior to earthquake unloading
195 using different outer wedge widths ranging from 25% to 0% of the full wedge width. Stress transfer
196 during earthquake unloading was determined by differencing the σ_m field from pre- to post-
197 earthquake. The corresponding distortional strain field also is examined for each simulation to
198 observe the internal deformation. Details about how the σ_m and the distortional strain invariant
199 fields are calculated can be found in our previous studies (Morgan, 2015; Wang and Morgan, 2019).
200 The following plots show distortional strain invariant field, stress, and seafloor uplift.
201

202 3.1.1 Landward Splay Fault Activity

203 The final states of simulations with the 45° landward dipping splay fault are plotted in
204 Figure 2. As shown in the left panel, σ_m within the inner wedge decreases (blue) during the
205 earthquake, whereas σ_m rises (red) in the region of the outer wedge close to the transition zone.
206 The outer wedge width decreases from Figures 2a to 2d, resulting in a progressive decrease in the
207 area of increased σ_m. This pattern demonstrates that the narrower the outer wedge, the easier it is

for coseismic ruptures to propagate to the toe. The distortional invariant plots, shown in right panels of Figure 2, exhibit a corresponding trend, reflected in variations in displacement along the splay fault with decreasing outer wedge width. The splay fault favors thrust faulting when there is a large outer wedge (Figure 2e) but exhibits normal displacement when the outer wedge width is very small (Figures 2g and 2h). In general, Figures 2e to 2h show a progressive transition from the thrust sense of slip to the normal sense of slip.

3.1.2 Seaward Splay Faults

The final states of simulations with the 45° seaward dipping splay fault are shown in Figure 3, and are very similar to those with the landward splay faults. σ_m decreases across the inner wedge and rises near boundary with the outer wedge. The area of reduced σ_m decreases as the outer wedge decreases (Figures 3a to 3d). When the outer wedge is very small, the stress decreases through the entire wedge. However, in contrast to the models with landward splay faults (Figures 2e and 2h), there is no evidence of normal sense of shear along any of the seaward dipping splay faults, and very little fault displacement occurs with very small outer wedges (Figures 3g and 3h). Interestingly, the presence of larger outer wedges (velocity-strengthening zone) can also cause the formation of new landward thrust faults (Figure 3e).

3.2 Effect of Outer Wedge Width on Seafloor Uplift

We measure seafloor uplift for each simulation by comparing the pre-earthquake and final wedge surface, using vertical displacement of the wedge surface parallel to gravity. This uplift, presumed to occur during the earthquake, is a direct indicator of tsunami potential. We apply a median filter to smooth perturbations in the uplift distribution introduced by the discrete nature of the DEM particle assemblage. The result reveals systematic variations in uplift that correlate with variations in the outer wedge width (Figure 4). For both landward and seaward dipping splay faults, the thickest part of the wedge exhibits subsidence (negative uplift), with progressively increasing uplift in the seaward direction. Small variations in the uplift profiles are evident in the vicinity of the splay faults, however, the greatest variations occur in association with the width of the outer wedge.

The largest outer wedge width results in significantly reduced seafloor uplift near the toe, whereas seafloor uplift peaks near the toe in the absence of an outer wedge. Thus, regardless of

fault dip (Figures 4a and 4b), the outer wedge (velocity-strengthening zone) width correlates inversely with the tsunami potential in the frontal wedge.

3.3 Effect of Fault Dip on Strain and Seafloor Uplift

The second set of simulations using Setup 1 were conducted for two fixed outer wedge widths at 0% and 25% of the full wedge width, and with different splay fault orientations. The distortional strain invariant fields are plotted for each case in Figure 5. Two reference models are shown without splay faults (Figures 5a and 5h). In the case of no outer wedge (Figure 5a), small normal-type shear zones are evident at very shallow depths and close to the wedge toe, indicating extension across the wedge. In the case of the 25% outer wedge (Figure 5h), a small thrust fault developed at the outer to inner wedge transition (~50 km). As a result of earthquake unloading, splay faults within the wedges lacking an outer wedge essentially showed very small activation (Figures 2h, 3h, 5c, 5e) or no activation (Figures 5b, 5d, 5f, 5g). In contrast, splay faults within the models with large outer wedge all exhibited some activation (Figures 2e, 3e, and 5i to 5n). The landward dipping splay faults were all activated as thrust faults (Figures 2e, 5i, 5j, 5k). The seaward dipping splay faults (Figures 3e, 5l, 5m, 5n) also exhibits apparent activation as thrust faults. Essentially, the models with prescribed splay faults show different degrees of activation depending on the fault dips as well as outer wedge width.

Seafloor uplifts are also calculated for all of the cases shown in Figure 6. In general, seafloor uplifts for models with landward splay faults and with seaward splay faults are essentially identical. The curves for models with landward splay faults are slightly separated near the wedge toes (Figures 6a and 6c), whereas the curves for the models with seaward splay faults mostly overlap (Figures 6b and 6d). Compared to the outer wedge width (Figure 4), therefore, splay fault dips have a very limited effect on seafloor uplift.

4 Applications to the Maule and Tohoku Earthquakes

We used Setup 2 to refine our previous simulations that sought to match published slip distributions for the 2010 Maule earthquake (Moreno *et al.*, 2012; Wang *et al.*, 2020) and 2011 Tohoku-oki earthquake (Sun *et al.*, 2017), respectively. Our previous investigation showed that the magnitude of peak fault slip has an inverse relationship with outer wedge (Wang *et al.*, 2021).

That study also provided important constraints for the best-fit widths of the outer wedges in each location, and we use similar values for this study. Therefore, our coseismic slip distributions for simplified models with no splay faults (black dotted curves in Figures 7 and 8) yield consistent peak slip values with those obtained for the Maule and Tohoku coseismic segments(Wang *et al.*, 2021). Here, we investigate the influence of the megasplay faults on the coseismic rupture extents and tsunami potential. We conduct multiple simulations, prescribing splay faults with different friction coefficients (Table S1) before the start of earthquake unloading stage.

4.1 2010 Maule Earthquake

Previous interpretations based on the tomographic model for the 2010 Mw 8.8 Maule earthquake rupture segment (Contreras-Reyes *et al.*, 2010; Contreras-Reyes *et al.*, 2017), show the outer wedge zone to be relatively large. The derived slip distributions for the 2010 Maule earthquake (Moreno *et al.*, 2012; Wang *et al.*, 2020) is shown in pink band and dashed curve in Figure 7b. The modeled peak slip is nearly 20 m, and is located ~90 km from the trench. Our simulation without a splay fault reproduces this peak and its position reasonably well (black dotted curve in Figure 7b). We then introduce an 80° seaward dipping splay fault that resembles the thrust-type Santa Maria fault system in the Maule segment (Figure 7a). Based on the interpreted profile by Melnick *et al.* (2012), the root of the splay fault presumably overlaps the updip end of the seismogenic zone (inner wedge). The friction coefficient along the splay fault is not known, so different values are tested in these simulations.

As shown in Figures 7b to 7c, the presence of pre-existing high-angle splay faults with any friction coefficient has minimal effect on the earthquake slip distribution. Likely, the large outer wedge (velocity-strengthening zone) in the Maule rupture zone (Contreras-Reyes *et al.*, 2010; Wang *et al.*, 2021) reduces fault activation and suppresses associated changes in slip. All of the models exhibit a prominent zone of high slip as well as large seafloor uplift at ~90 km (Figures 7b to 7e), which is attributed to the contrasting friction condition at the boundary between outer and inner wedge. This transition zone between the inner and outer wedges induces compression during the earthquake unloading, causing localized uplift and subsidence. This displacement is slightly enhanced by the presence of a splay fault and varies with fault friction. Uplift of the hanging wall (<90 km), and subsidence of the footwall (>90 km) is greatest for the lowest values of friction (Figure 7e), and most pronounced above the footwall. The tiny differences among the cases

suggest that splay fault activation along the Maule rupture segment will have minor effect on the tsunami potential in this area.

4.2 2011 Tohoku Earthquake

The 2011 Tohoku earthquake rupture segment is known to have experienced a trench breaking rupture with over 60 m peak slip (Wei *et al.*, 2012; Sun *et al.*, 2017). According to previous studies, a landward splay fault was reactivated by the 2011 Tohoku earthquake (Tsuji *et al.*, 2011). We, therefore, construct a model with a landward splay fault and a very small outer wedge (Figure 8a), based on the published seismic profile by (Ito *et al.*, 2011; Tsuji *et al.*, 2011). Our model without a splay fault (black dotted curve in Figure 8b) yielded a peak slip of about 64 m close to the trench, which is reasonably consistent with the derived slip distributions (pink band and dashed curve in Figure 8b) for the 2011 Tohoku earthquake (Sun *et al.*, 2017; Wang *et al.*, 2021).

We also explore here how the presence of a landward dipping splay fault might affect the rupture extent and tsunami size. We fix the fault dip at 30°, comparable to the seismic interpretation (Tsuji *et al.*, 2011), and examine different friction values along the fault. Figure 8c shows that the coseismic megathrust fault slip and its amplitude are affected moderately by the friction along the splay fault. The separation between the model without a splay fault (black dotted curve in Figure 8c) and the various faulted models (blue, red and green curves in Figure 8c) demonstrates that displacement along the splay fault can accommodate some of the coseismic slip along the decollement, reducing displacement at the toe of the wedge.

As shown in Figure 8d, the splay fault also results in increased uplift near where it emerges at the top of the wedge. Lower friction values along the splay fault correspond with increased uplift of the hanging wall of the landward splay fault during earthquake unloading (Figure 8e). However, fault friction seems to have only a moderate effect on the tsunami potential in the Tohoku area.

5 Discussion

5.1 Relationship among Outer Wedge Width, Splay Fault Activity, and Tsunami Potential

Previous studies show the strong control of the width of the outer wedge (velocity strengthening zone) on the rupture extents and slip distribution (Contreras-Reyes *et al.*, 2010; Wang *et al.*, 2021). Consistent with that finding, our first set of simulations of non-cohesive models also demonstrates that the width of the velocity-strengthening outer wedge affects the stress and

strain along the splay fault (Figures 2 and 3). Based on our numerical results (Figures 2 and 3), it is likely that different splay fault activities along different rupture segments triggered by the same seismic event (Lieser *et al.*, 2014) may be due to variations in outer wedge width along the margin. The width of the outer wedge gradually increases from south to north of the Maule segment along the SC Chile Margin (Contreras-Reyes *et al.*, 2017). Splay fault activity during the 2010 Maule earthquake also appears to have increased from south to north (Lieser *et al.*, 2014), which is consistent with our numerical results (Figures 2e to 2g).

Furthermore, our analysis of seafloor uplift (Figure 4) shows that, to the first order, the width of the outer wedge may inversely correlate with the seafloor uplift. Interestingly, if the outer wedge is sufficiently small, a normal splay fault can be activated during a megathrust earthquake. However, the amount of displacement on a normal fault is lower than that on thrust splay faults (Figures 2 and 3). Therefore, if significant thrust activity occurs along a splay fault, this may imply the presence of a wide outer wedge, reducing the tsunami potential locally (Figure 4).

5.2 Effects of Megasplay Fault Properties on Seismic Hazard

Based on our first set of simplified models using different splay fault dips with the same values of fault friction, we demonstrate that variations in dip can affect the stress and strain along the splay fault during the unloading phase (Figure 5), however, we see relatively insignificant differences in the seafloor uplift (Figure 6). Thus, compared to the width of the outer wedge, variations in megasplay fault dip are unlikely to significantly affect tsunami potential. We attribute this result to the fact that wedge preconditioning results in similar initial stress states on the prescribed faults regardless of their orientation, limiting fault slip during unloading. If the splay faults existed prior to the preconditioning, they would have accumulated different levels of deformation and stress during loading, which might be reflected in differences in slip during unloading. In our second set of models, however, we prescribe the splay fault with a fixed dip for each simulation case, and test different values of friction coefficient along the splay fault. The differences in seafloor uplift can be explained by increasing ease of fault slip with lower friction coefficients during earthquake unloading.

According to our simulation results for the 2010 Maule earthquake (Figure 7), the predominant factor that controls the rupture extent and tsunami size is the width of the velocity-strengthening outer wedge. If the width of the outer wedge (velocity-strengthening zone) is

relatively large (Contreras-Reyes *et al.*, 2010; Wang *et al.*, 2021), the friction of the seaward splay fault does not contribute much to the coseismic rupture extent and tsunami potential in the Maule rupture zone (Figures 7b and 7d), and the coseismic displacements along the splay are very small.

Interestingly, the friction on the landward-dipping splay fault contributes moderately to the magnitude of the coseismic rupture and tsunami potential in the Tohoku rupture zone (Figures 8b and 8d), which has a very small outer wedge (velocity strengthening zone) and experienced trench breaking rupture during the earthquake (Wang and Tréhu, 2016). As noted above, if we had included the splay fault prior to the wedge loading phase, it might have experienced more displacement during earthquake unloading, better matching field observations from the Tohoku earthquake itself.

In general, our simulation results demonstrate that the effects of megasplay faults, during earthquake unloading, are limited. Our simulation results show that the presence of megasplay normal faults and their reactivation may not necessarily contribute to large earthquake size and tsunami potential in the Tohoku rupture zone. Likely, a more critical factor is the change in basal friction along the megathrust fault throughout the entire earthquake cycle. The properties of the splay fault are second-order factors that may moderately influence the rupture extents and tsunami size. This finding suggests that coseismic normal fault slip in the Shumagin Gap may not have played as significant a role in rupture extent or tsunamigenesis as has been suggested by others (Bécel *et al.*, 2017).

6 Conclusions

We carried out two sets of simulations to examine the effects of spay fault dips on rupture extents and seafloor uplift. Our first set of simulations using non-cohesive models, demonstrates that the width of velocity-strengthening outer wedge along the margin has the greatest effect on splay fault activity and thus on tsunami generation at different localities. The variations in outer wedge width (velocity-strengthening zone) along strike in the Maule rupture zone can help explain the different splay fault activities observed at different localities during the 2010 event.

In the second part of the study, we build more realistic cohesive models to assess the effects of splay faults on simulated megathrust displacements, which may better match published coseismic slip distributions for the 2010 Maule and 2011 Tohoku earthquakes. Different values of friction coefficient along the splay fault plane can lead to different amounts of displacement along

the splay fault during earthquake unloading. However, our simulation results indicate that the earthquake rupture extent and tsunami potential are predominantly controlled by friction variations along the megathrust fault, governed by outer wedge (velocity-strengthening zone) width, rather than friction along the megasplay fault. Our numerical results demonstrate that activation of a megasplay fault likely had minimal effect on earthquake coseismic rupture and tsunami potential during the 2010 Maule rupture, but could have had a moderate effect during the 2011 Tohoku rupture.

Our results show the presence of megasplay normal faults does not necessarily imply significant seismic hazards in a subduction system. The effect of megasplay fault dip and its corresponding coseismic displacements along the splay fault on rupture extents and tsunami genesis is limited. We suggest that the properties of the splay fault are second-order factors affecting coseismic slip distribution and tsunami potential, whereas the key factor is the variation in basal friction along the megathrust fault.

Acknowledgments and Data

This work was funded in part by National Science Foundation grant EAR-1723249. Computing facilities were made available in part through the Rice Center for Computational Geophysics. The author benefitted from discussion about modeling and subduction system with my colleagues. Interested parties are encouraged to contact the author to request copies of animated GIFs of the simulations for further study. The modeling results, corresponding files, raw data, and sample code for this research can be found in https://doi.org/10.6084/m9.figshare.15122229.v1.

References

Bécel, A., Shillington, D. J., Delescluse, M., Nedimović, M. R., Abers, G. A., Saffer, D. M., Webb, S. C., Keranen, K. M., Roche, P.-H., and Li, J. (2017), Tsunamigenic Structures in a Creeping Section of the Alaska Subduction Zone, *Nature Geoscience*, *10*(8), 609-613.

Contreras-Reyes, E., Maksymowicz, A., Lange, D., Grevemeyer, I., Muñoz-Linford, P., and Moscoso, E. (2017), On the Relationship between Structure, Morphology and Large Coseismic Slip: A Case Study of the Mw 8.8 Maule, Chile 2010 Earthquake, *Earth and Planetary Science Letters*, *478*, 27-39.

Contreras-Reyes, E., Flueh, E. R., and Grevemeyer, I. (2010), Tectonic Control on Sediment Accretion and Subduction Off South Central Chile: Implications for Coseismic Rupture Processes of the 1960 and 2010 Megathrust Earthquakes, *Tectonics*, *29*(6).

Grassi, B. (2021), Largest Earthquake in 50 Years: What We Know So Far, *Alaska Earthquake Center*, *earthquake.alaska.edu*.

Ito, Y., Tsuji, T., Osada, Y., Kido, M., Inazu, D., Hayashi, Y., Tsushima, H., Hino, R., and Fujimoto, H. (2011), Frontal Wedge Deformation near the Source Region of the 2011 Tohoku-Oki Earthquake, *Geophysical Research Letters*, *38*(7).

Lieser, K., Grevemeyer, I., Lange, D., Flueh, E., Tilmann, F., and Contreras-Reyes, E. (2014), Splay Fault Activity Revealed by Aftershocks of the 2010 Mw 8.8 Maule Earthquake, Central Chile, *Geology*, *42*(9), 823-826.

Lotto, G. C., Jeppson, T. N., and Dunham, E. M. (2019), Fully Coupled Simulations of Megathrust Earthquakes and Tsunamis in the Japan Trench, Nankai Trough, and Cascadia Subduction Zone, *Pure and Applied Geophysics*, *176*(9), 4009-4041.

Maksymowicz, A. (2015), The Geometry of the Chilean Continental Wedge: Tectonic Segmentation of Subduction Processes Off Chile, *Tectonophysics*, *659*, 183-196.

McKenzie, D., and Jackson, J. (2012), Tsunami Earthquake Generation by the Release of Gravitational Potential Energy, *Earth and Planetary Science Letters*, *345*, 1-8.

Melnick, D., Bookhagen, B., Echtler, H. P., and Strecker, M. R. (2006), Coastal Deformation and Great Subduction Earthquakes, Isla Santa María, Chile (37 S), *Geological Society of America Bulletin*, *118*(11-12), 1463-1480.

Melnick, D., Moreno, M., Motagh, M., Cisternas, M., and Wesson, R. L. (2012), Splay Fault Slip During the Mw 8.8 2010 Maule Chile Earthquake, *Geology*, *40*(3), 251-254.

Moore, G., Bangs, N., Taira, A., Kuramoto, S., Pangborn, E., and Tobin, H. (2007), Three-Dimensional Splay Fault Geometry and Implications for Tsunami Generation, *Science*, *318*(5853), 1128-1131.

Moreno, M., Melnick, D., Rosenau, M., Baez, J., Klotz, J., Oncken, O., Tassara, A., Chen, J., Bataille, K., and Bevis, M. (2012), Toward Understanding Tectonic Control on the Mw 8.8 2010 Maule Chile Earthquake, *Earth and Planetary Science Letters*, *321*, 152-165.

Moreno, M., Rosenau, M., and Oncken, O. (2010), 2010 Maule Earthquake Slip Correlates with Pre-Seismic Locking of Andean Subduction Zone, *Nature*, *467*(7312), 198-202.

Morgan, J. K. (2015), Effects of Cohesion on the Structural and Mechanical Evolution of Fold and Thrust Belts and Contractional Wedges: Discrete Element Simulations, *Journal of Geophysical Research: Solid Earth*, *120*(5), 3870-3896.

Olsen, K. M., Bangs, N. L., Tréhu, A. M., Han, S., Arnulf, A., and Contreras-Reyes, E. (2020), Thick, Strong Sediment Subduction Along South-Central Chile and Its Role in Great Earthquakes, *Earth and Planetary Science Letters*, *538*, 116195.

Polet, J., and Kanamori, H. (2000), Shallow Subduction Zone Earthquakes and Their Tsunamigenic Potential, *Geophysical Journal International*, *142*(3), 684-702.

Ruppert, N. A., and Gardine, L. (2021), 2020 Alaska Seismicity Summary.

Sun, T., Wang, K., Fujiwara, T., Kodaira, S., and He, J. (2017), Large Fault Slip Peaking at Trench in the 2011 Tohoku-Oki Earthquake, *Nature communications*, *8*(1), 1-8.

Tsuji, T., Ito, Y., Kido, M., Osada, Y., Fujimoto, H., Ashi, J., Kinoshita, M., and Matsuoka, T. (2011), Potential Tsunamigenic Faults of the 2011 Off the Pacific Coast of Tohoku Earthquake, *Earth, planets and space*, *63*(7), 58.

Wang, K., Brown, L., Hu, Y., Yoshida, K., He, J., and Sun, T. (2019), Stable Forearc Stressed by a Weak Megathrust: Mechanical and Geodynamic Implications of Stress Changes Caused by the M= 9 Tohoku-Oki Earthquake, *Journal of Geophysical Research: Solid Earth*, *124*(6), 6179-6194.

Wang, K., and Hu, Y. (2006), Accretionary Prisms in Subduction Earthquake Cycles: The Theory of Dynamic Coulomb Wedge, *Journal of Geophysical Research: Solid Earth*, *111*(B6).

Wang, K., Huang, T., Tilmann, F., Peacock, S. M., and Lange, D. (2020), Role of Serpentinized Mantle Wedge in Affecting Megathrust Seismogenic Behavior in the Area of the 2010 M= 8.8 Maule Earthquake, *Geophysical Research Letters*, *47*(22), e2020GL090482.

Wang, K., and Tréhu, A. M. (2016), Invited Review Paper: Some Outstanding Issues in the Study of Great Megathrust Earthquakes—the Cascadia Example, *Journal of Geodynamics*, *98*, 1-18.

Wang, X., and Morgan, J. K. (2019), Controls on Fore-Arc Deformation and Stress Switching after the Great 2011 Tohoku-Oki Earthquake from Discrete Numerical Simulations, *Journal of Geophysical Research: Solid Earth*, *124*(8), 9265-9279.

Wang, X., Morgan, J. K., and Bangs, N. (2021), Relationships among Forearc Structure, Fault Slip, and Earthquake Magnitude: Numerical Simulations with Applications to the Central Chilean Margin, *Geophysical Research Letters*, *48*(13), e2021GL092521.

Wei, S., Graves, R., Helmberger, D., Avouac, J.-P., and Jiang, J. (2012), Sources of Shaking and Flooding During the Tohoku-Oki Earthquake: A Mixture of Rupture Styles, *Earth and Planetary Science Letters*, *333*, 91-100.

Wendt, J., Oglesby, D. D., and Geist, E. L. (2009), Tsunamis and Splay Fault Dynamics, *Geophysical Research Letters*, *36*(15).

Figure Captions

Figure 1 DEM Model Setup. The lower plate in gray is fixed while the upper plate in orange or yellow moves above it. The virtual splay fault plane (black line) is defined by prescribing different interparticle friction coefficients at contacts, and the plane dip can be varied and pre-defined. Details about the particle contacts and surface type pre-assignments can be found in the supplementary material (S1).

Figure 2 Effect of outer wedge width on stress and strain in models with 45° landward dipping splay fault with friction coefficient of zero. (a)-(d) Simulated coseismic changes in mean stress field for each earthquake, denoting stress transfer within the wedge; red indicates increase in mean stress; blue indicates decrease. (e)-(h) Cumulative distortional strain invariant field for each case. Black dashed lines indicate splay fault boundaries. Blue dashed lines represent range of outer wedge. Gray triangles indicate the roots of the splay faults.

Figure 3 Effect of outer wedge width on stress and strain in the model with 45° seaward dipping splay fault. (a)-(d) Simulated coseismic changes in mean stress field for each earthquake. (e)-(h) Cumulative distortional strain invariant field for each case. Colors and symbols are the same as in Figure 2.

Figure 4 Effect of outer wedge width on seafloor uplift. (a) Seafloor uplifts for 45° landward splay fault dip. (b) Seafloor uplifts for 45° seaward splay fault dip. Blue dashed lines represent the outer wedge widths. Gray triangles indicate the roots of the splay faults.

Figure 5 Effect of splay fault dip and interaction with outer wedge on strain. Cumulative distortional strain invariant fields for models with no outer wedge (a)-(g) and ones with large outer wedges (h)-(n). Blue dashed lines represent outer wedge widths. Gray triangles indicate the roots of the splay faults.

Figure 6 Effect of splay fault dips on seafloor uplift. (a) Seafloor uplift for models with landward splay faults without an outer wedge. (b) Seafloor uplift for models with seaward splay faults without an outer wedge. (c) Seafloor uplift for models with landward splay faults with large outer wedges. (d) Seafloor uplift for models with seaward splay faults with large outer wedges. The blue dashed lines represent the outer wedge dimension. Gray triangles locate the roots of the splay faults.

Figure 7 Coseismic rupture and seafloor uplift for 2010 Maule earthquake from simulations. (a) Initial wedge setup (before the preconditioning stage) resembles the wedge profile with the crustal structure of Santa Maria Fault System in SC Chile Margin near the epicenter of the 2010 Maule earthquake (Melnick *et al.*, 2012). Wedge supports an 80° seaward splay fault and large outer wedge. (b) Simulated slip distributions, compared to range of slip models from Wang *et al.* (2020) shown in pink shading. (c) Enlargement of slip distributions within the gray box shown in (b). (d) Simulated seafloor uplift. (e) Enlargement of uplift shown in the gray box in (d). The dashed orange lines show the geometry of the upper plate, and the solid orange line denotes the position of the splay fault plane.

Figure 8 Coseismic rupture and seafloor uplift for 2010 Tohoku earthquake from simulations. (a) Initial wedge setup, modeled after interpreted seismic reflection profile near the hypocenter of the 2011 Tohoku-oki earthquake, with 30° landward splay fault and small outer wedge (Tsuji *et al.*, 2011). (b) Simulated slip distributions, compared to the preferred range of slip models from Sun *et al.* (2017) shown in pink shading. (c) Enlargement of slip distributions shown in gray box in (b). (d) Simulated seafloor uplift. (e) Enlargement of uplift shown in the gray box in (d). The dashed orange lines show the geometry of the upper plate, and the solid orange line denotes the position of the splay fault plane.

Figure1.

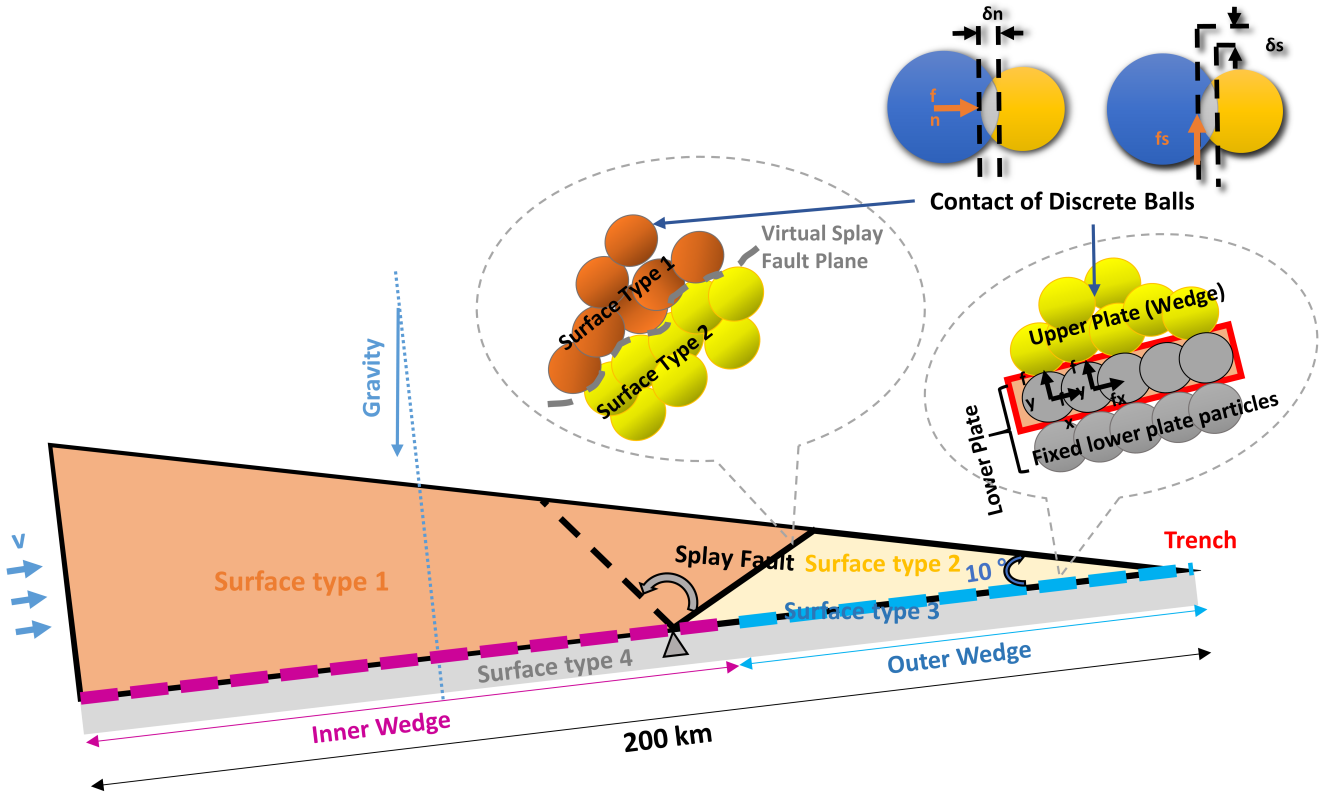
δn
δs
fn
fs
Contact of Discrete Balls
Virtual Splay
Fault Plane
Surface Type 1
Surface Type 2
Upper Plate (Wedge)
Lower Plate
Fixed lower plate particles
Gravity
V
Surface type 1
Splay Fault
Surface type 2
10 °
Trench
Surface type 3
Surface type 4
Outer Wedge
Inner Wedge
200 km

Figure2.

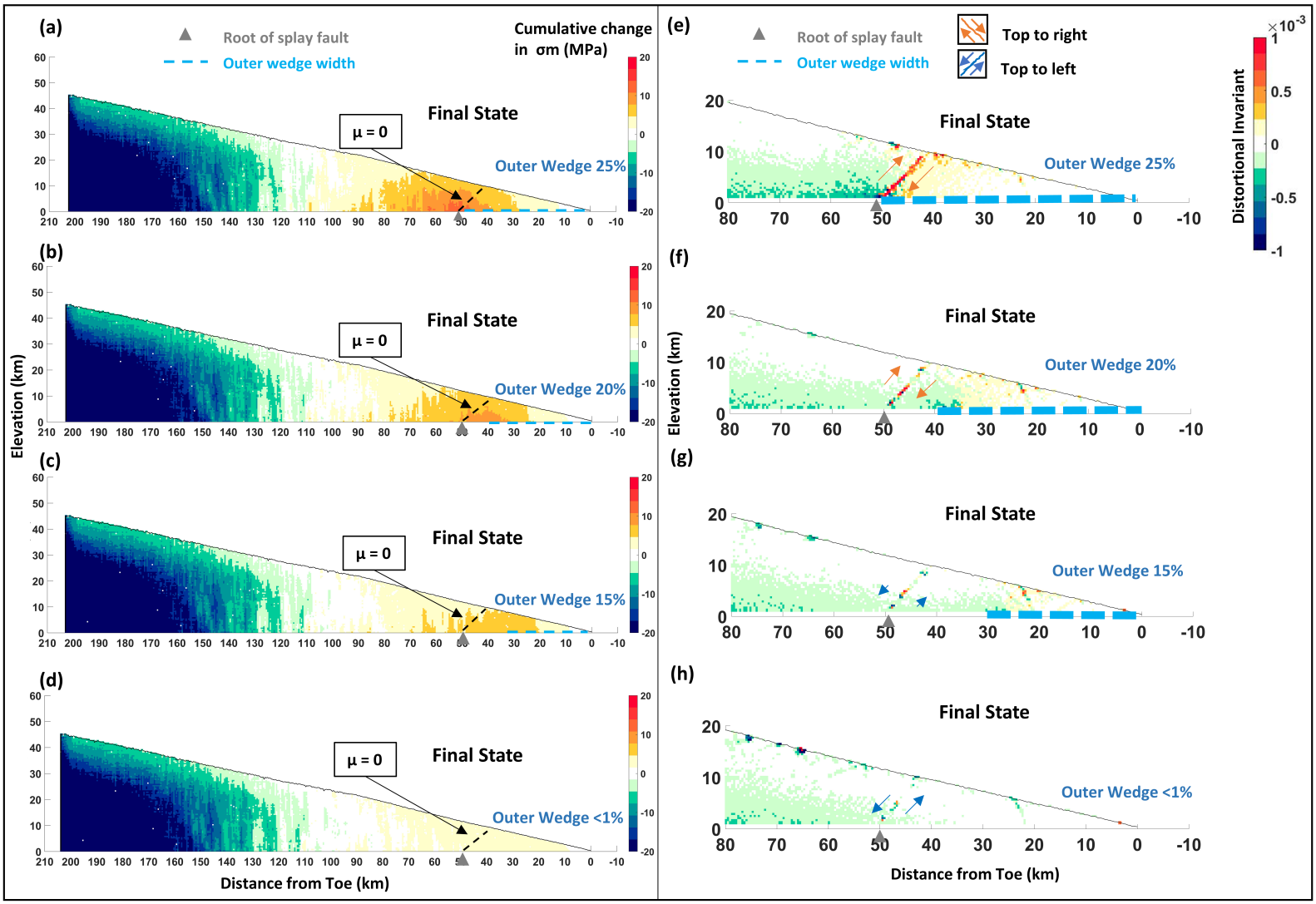
(a)
Root of splay fault
Outer wedge width
Cumulative change in σm (MPa)
μ = 0
Final State
Outer Wedge 25%
(b)
μ = 0
Final State
Outer Wedge 20%
(c)
μ = 0
Final State
Outer Wedge 15%
(d)
μ = 0
Final State
Outer Wedge <1%
Elevation (km)
Distance from Toe (km)
(e)
Root of splay fault
Outer wedge width
Top to right
Top to left
Final State
Outer Wedge 25%
Distortional Invariant
(f)
Final State
Outer Wedge 20%
(g)
Final State
Outer Wedge 15%
(h)
Final State
Outer Wedge <1%
Distance from Toe (km)

Figure3.

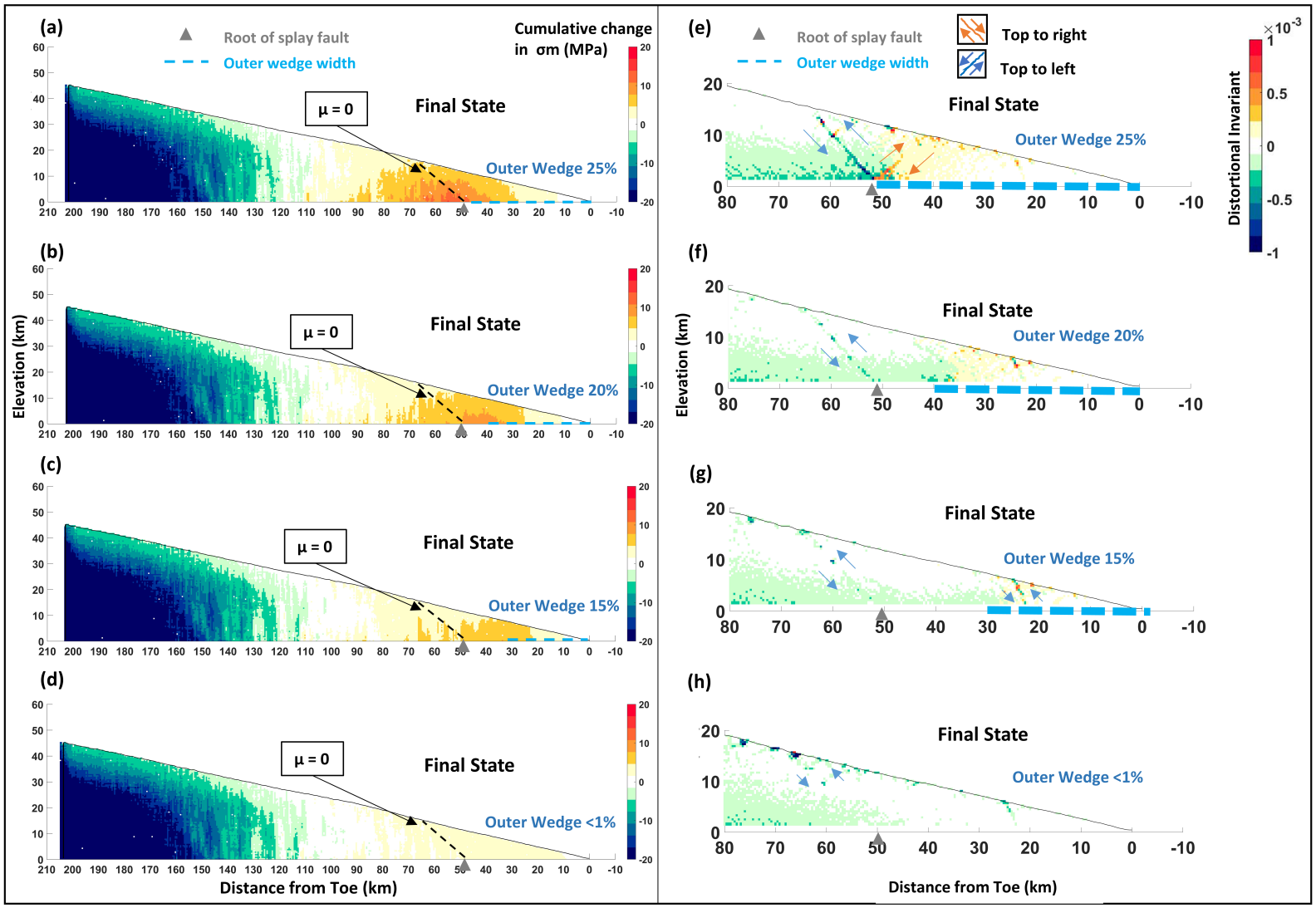
(a)
Root of splay fault
Outer wedge width
Cumulative change in σm (MPa)
μ = 0
Final State
Outer Wedge 25%
(b)
μ = 0
Final State
Outer Wedge 20%
(c)
μ = 0
Final State
Outer Wedge 15%
(d)
μ = 0
Final State
Outer Wedge <1%
Elevation (km)
Distance from Toe (km)
(e)
Root of splay fault
Outer wedge width
Top to right
Top to left
Final State
Outer Wedge 25%
Distortional Invariant
×10-3
(f)
Final State
Outer Wedge 20%
(g)
Final State
Outer Wedge 15%
(h)
Final State
Outer Wedge <1%
Elevation (km)
Distance from Toe (km)

Figure4.

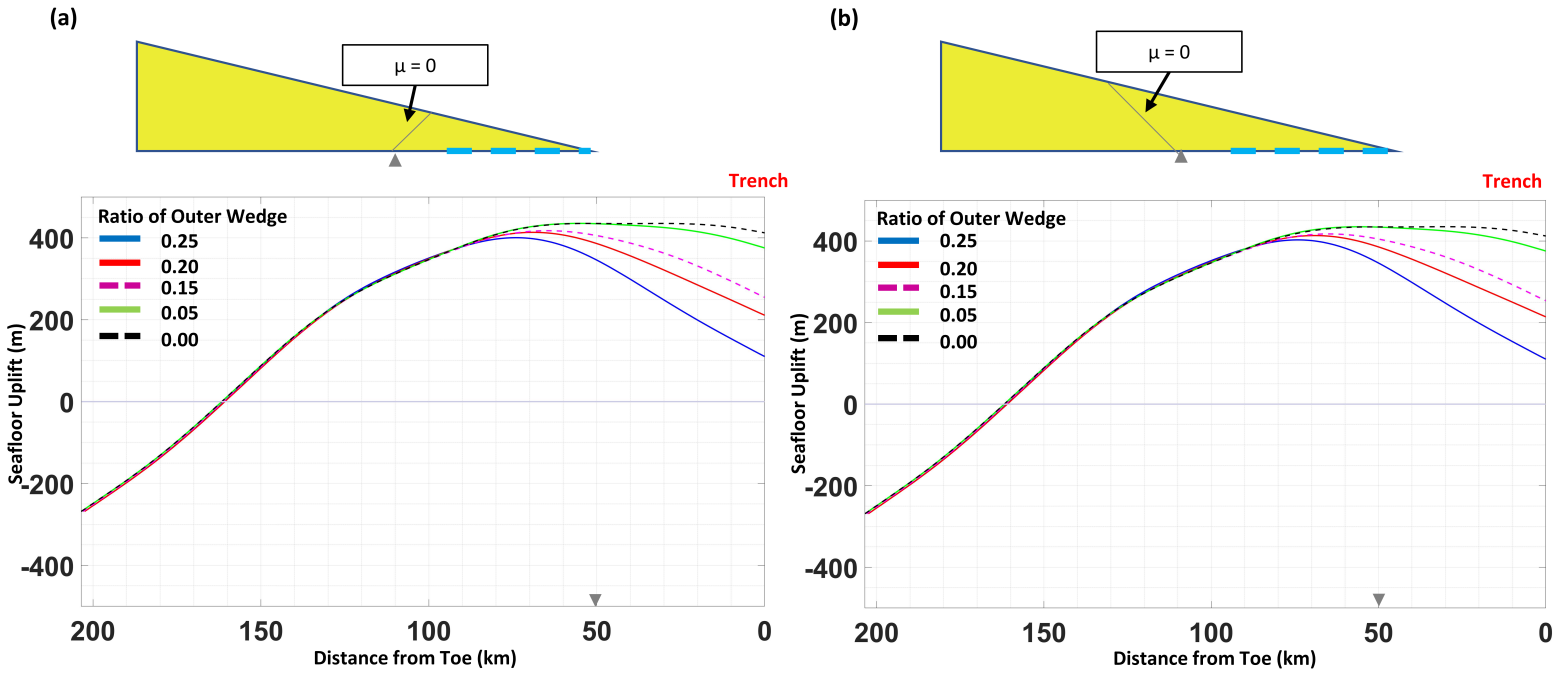
(a)
μ = 0
Trench
Ratio of Outer Wedge
0.25
0.20
0.15
0.05
0.00
Seafloor Uplift (m)
400
200
0
-200
-400
200
150
100
50
0
Distance from Toe (km)
(b)
μ = 0
Trench
Ratio of Outer Wedge
0.25
0.20
0.15
0.05
0.00
Seafloor Uplift (m)
400
200
0
-200
-400
200
150
100
50
0
Distance from Toe (km)

Figure5.

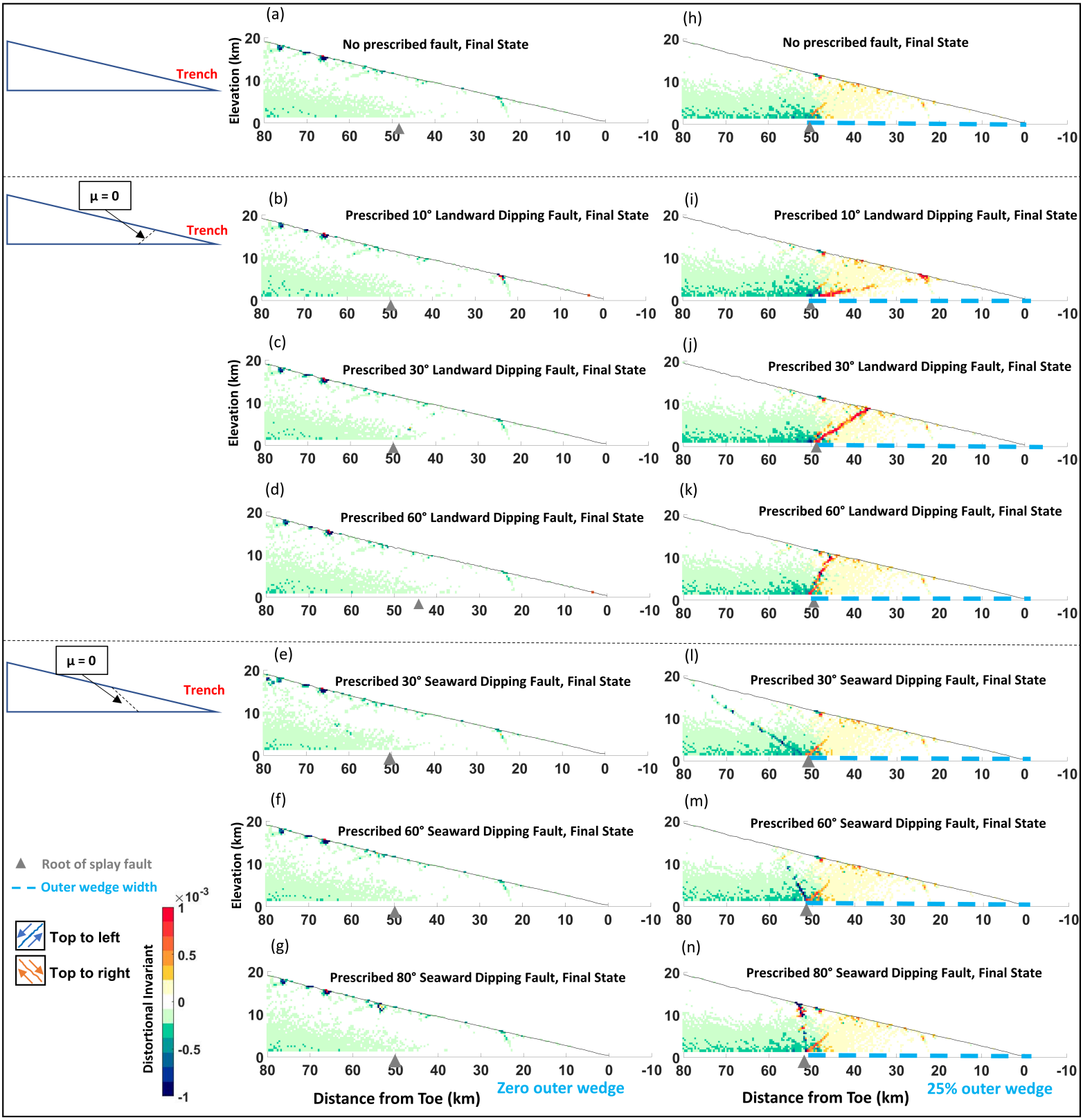
(a)
No prescribed fault, Final State
(h)
No prescribed fault, Final State
Trench
(b)
Prescribed 10° Landward Dipping Fault, Final State
(i)
Prescribed 10° Landward Dipping Fault, Final State
μ = 0
Trench
(c)
Prescribed 30° Landward Dipping Fault, Final State
(j)
Prescribed 30° Landward Dipping Fault, Final State
(d)
Prescribed 60° Landward Dipping Fault, Final State
(k)
Prescribed 60° Landward Dipping Fault, Final State
(e)
Prescribed 30° Seaward Dipping Fault, Final State
(l)
Prescribed 30° Seaward Dipping Fault, Final State
μ = 0
Trench
(f)
Prescribed 60° Seaward Dipping Fault, Final State
(m)
Prescribed 60° Seaward Dipping Fault, Final State
Root of splay fault
Outer wedge width
Top to left
Top to right
Distortional Invariant
(g)
Prescribed 80° Seaward Dipping Fault, Final State
(n)
Prescribed 80° Seaward Dipping Fault, Final State
Elevation (km)
Distance from Toe (km)
Zero outer wedge
Distance from Toe (km)
25% outer wedge

Figure6.

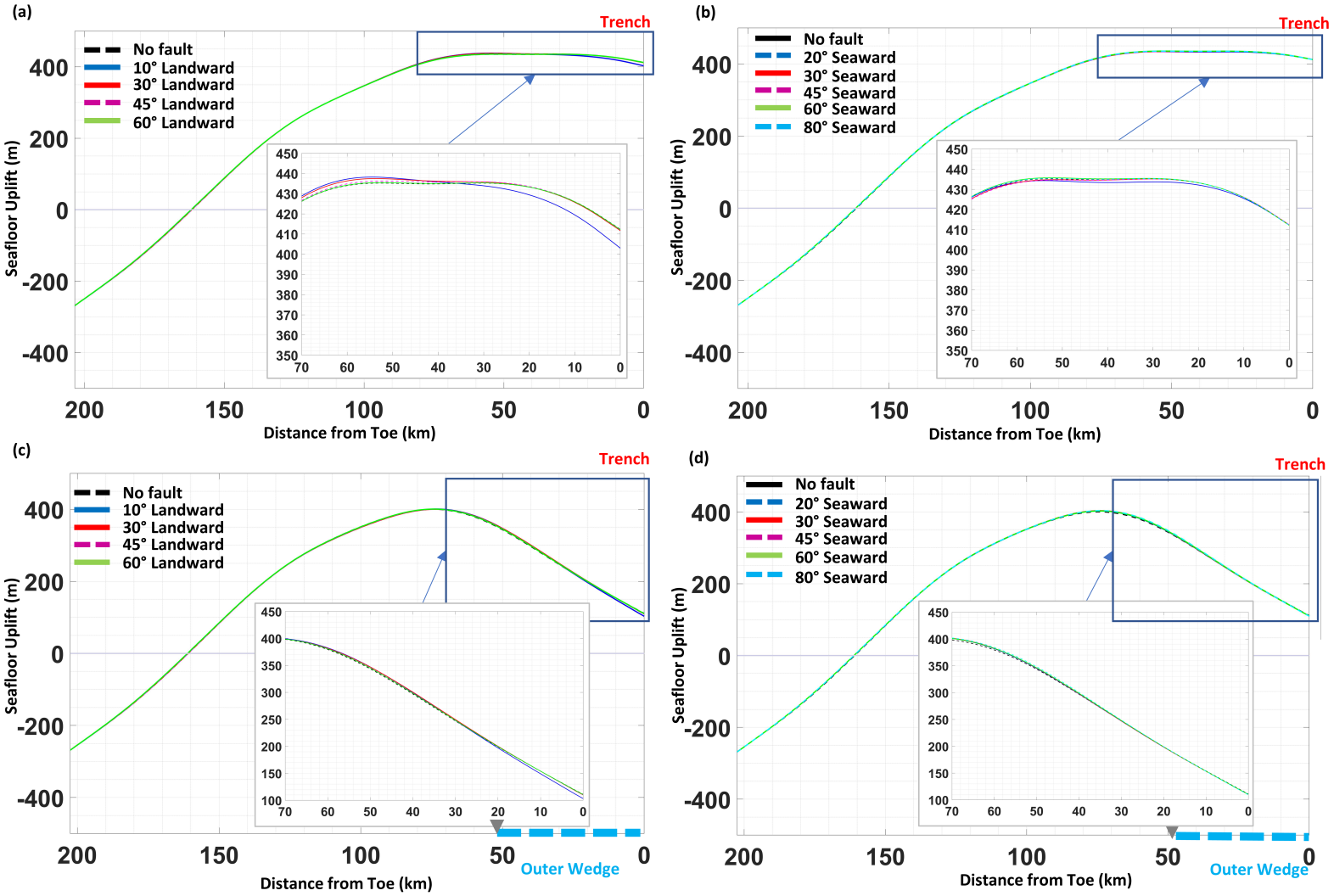
(a)
Trench
No fault
10° Landward
30° Landward
45° Landward
60° Landward
Seafloor Uplift (m)
Distance from Toe (km)
(b)
Trench
No fault
20° Seaward
30° Seaward
45° Seaward
60° Seaward
80° Seaward
Seafloor Uplift (m)
Distance from Toe (km)
(c)
Trench
No fault
10° Landward
30° Landward
45° Landward
60° Landward
Seafloor Uplift (m)
Distance from Toe (km)
Outer Wedge
(d)
Trench
No fault
20° Seaward
30° Seaward
45° Seaward
60° Seaward
80° Seaward
Seafloor Uplift (m)
Distance from Toe (km)
Outer Wedge

Figure7.

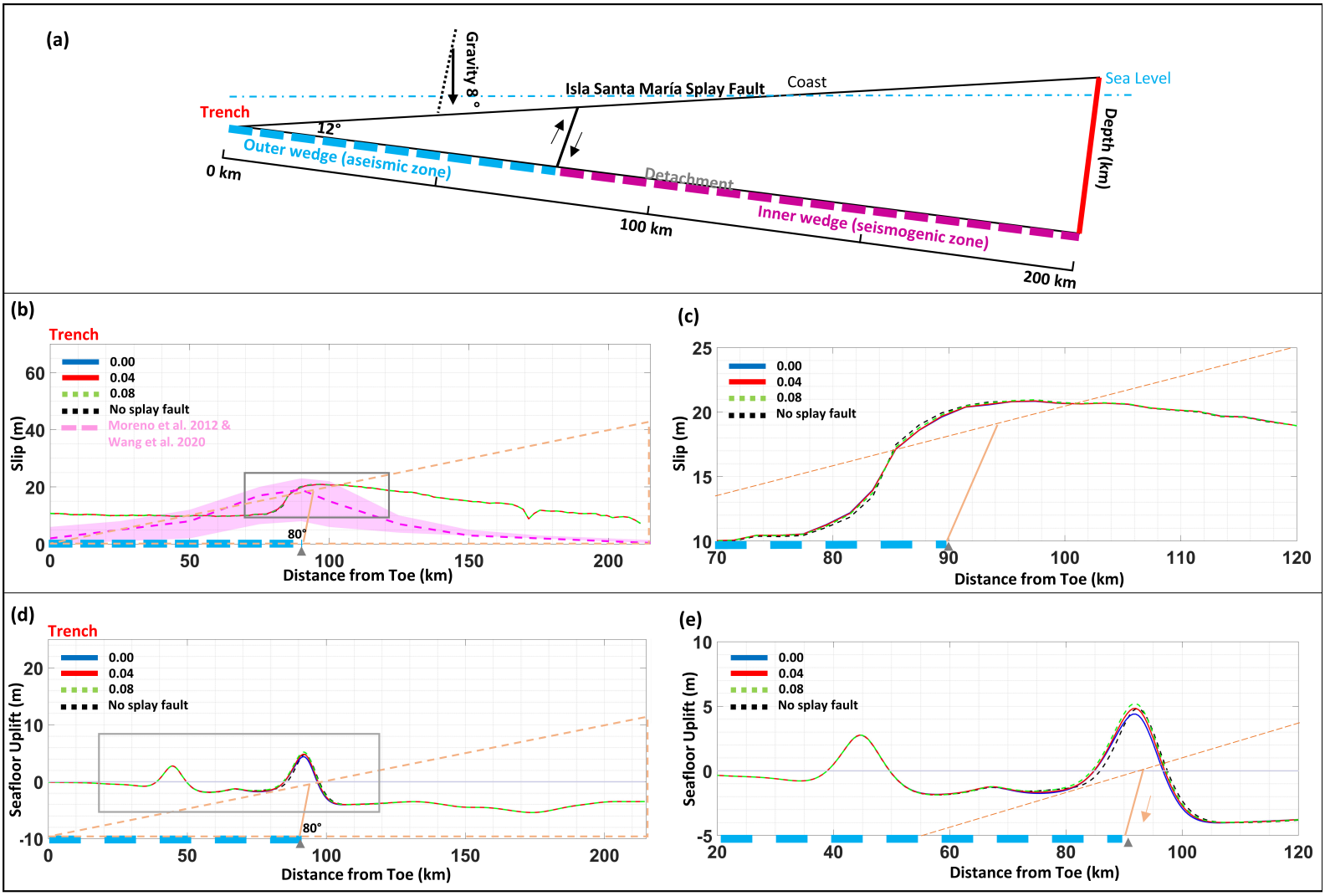
(a)
Gravity 8 °
Isla Santa María Splay Fault
Coast
Sea Level
Trench
12°
Outer wedge (aseismic zone)
Detachment
Inner wedge (seismogenic zone)
Depth (km)
0 km
100 km
200 km
(b)
Trench
0.00
0.04
0.08
No splay fault
Moreno et al. 2012 &
Wang et al. 2020
Slip (m)
80°
Distance from Toe (km)
(c)
0.00
0.04
0.08
No splay fault
Slip (m)
Distance from Toe (km)
(d)
Trench
0.00
0.04
0.08
No splay fault
Seafloor Uplift (m)
80°
Distance from Toe (km)
(e)
0.00
0.04
0.08
No splay fault
Seafloor Uplift (m)
Distance from Toe (km)

Figure8.

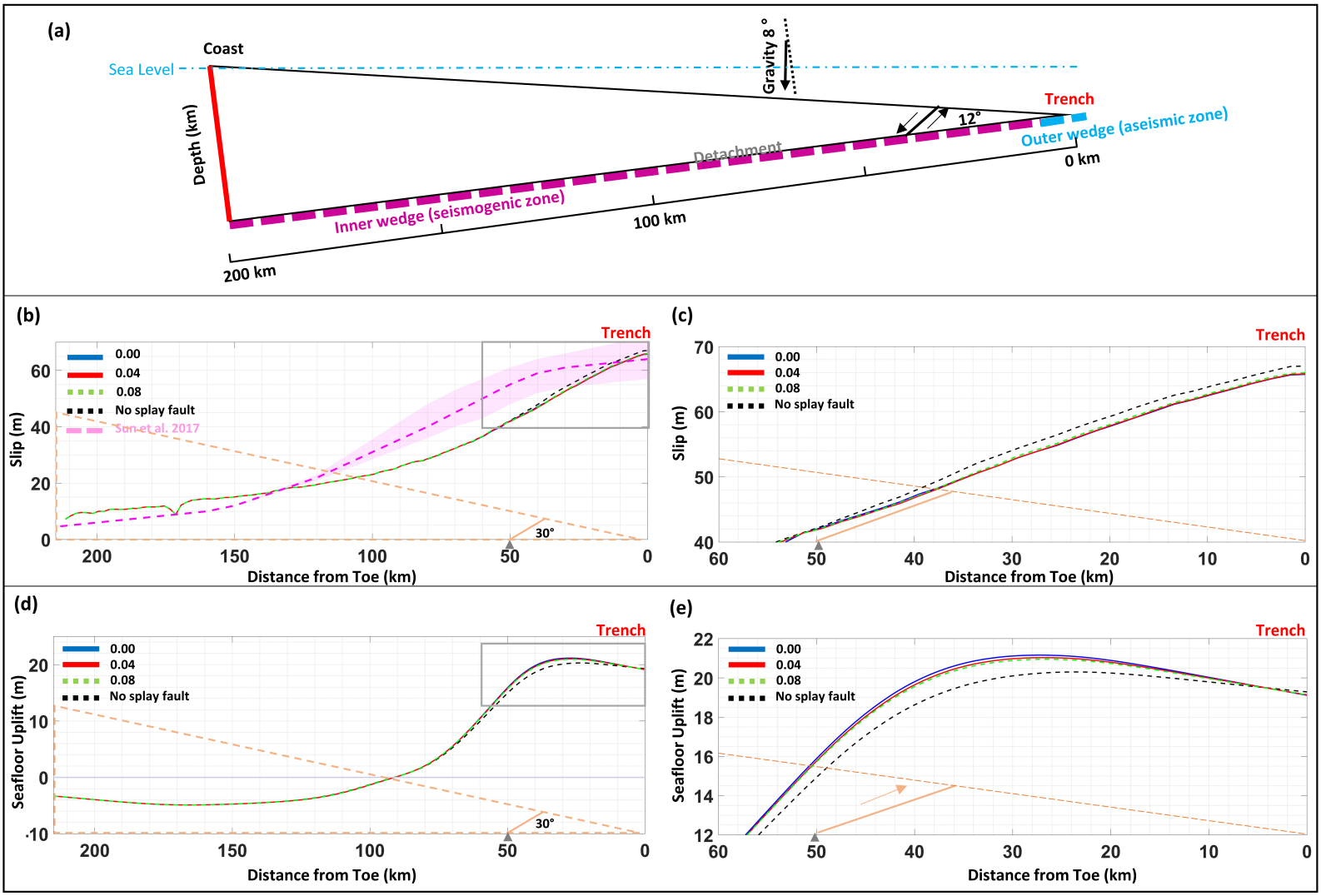
(a)
Coast
Sea Level
Depth (km)
Gravity 8 °
Trench
12°
Outer wedge (aseismic zone)
Detachment
0 km
Inner wedge (seismogenic zone)
100 km
200 km
(b)
Trench
0.00
0.04
0.08
No splay fault
Sun et al. 2017
Slip (m)
30°
Distance from Toe (km)
(c)
Trench
0.00
0.04
0.08
No splay fault
Slip (m)
Distance from Toe (km)
(d)
Trench
0.00
0.04
0.08
No splay fault
Seafloor Uplift (m)
30°
Distance from Toe (km)
(e)
Trench
0.00
0.04
0.08
No splay fault
Seafloor Uplift (m)
Distance from Toe (km)